CrossMark

ORIGINAL PAPER

İ. Özdemir

Resistive force theory-based analysis of magnetically driven slender flexible micro-swimmers

Abstract Resistive force theory is concise and reliable approach to resolve flow-induced viscous forces on submerged bodies at low Reynolds number flows. In this paper, the theory is adapted for very thin shell-type structures, and a solution procedure within a nonlinear finite element framework is presented. Flow velocity proportional drag forces are treated as configuration-dependent external forces and embedded in a commercial finite element solver (ABAQUS) through user element subroutine. Furthermore, incorporation of magnetic forces induced by external fields on magnetic subdomains of such thin-walled structures is addressed using a similar perspective without resolving the magnetic field explicitly. The treatment of viscous drag forces and the magnetic body couples is done within the same user element formalism. The formulation and the implementation are verified and demonstrated by representative examples including the bidirectional swimming of thin strips with magnetic ends.

1 Introduction

There is an increasing interest in the mechanics of swimming at microorganism length scales since man-made replicas of micro-swimmers might be very effective alternatives in emerging fields such as robotic surgery and targeted drug delivery [1].

At micrometer scale flows, the role of inertia forces is negligible, and the flow is essentially governed by the viscous forces resulting in low Reynolds number flow regime [2,3]. The physics of fluid–structure interaction (FSI) at this flow regime is substantially different from what is observed at high Reynolds number flows. In his seminal works dating back to early 1950s, Taylor presented a rigorous analysis of swimming sheets at low Reynolds number flows [4]. Soon after, a concise theory to compute hydrodynamic forces exerted by the fluid on the finite sized slender bodies was presented by Gray and Hancock [5] which is called the resistive force theory (RFT). In RFT, forces exerted on the slender deformable body by the surrounding fluid are described externally applied normal and tangential tractions with velocity proportional magnitudes. The proportionality constants are the so-called drag coefficients which typically show a strong anisotropy for slender bodies. This theory has been extensively used and tested against more refined theories such as slender body theory of Johnson [6], direct numerical simulation [7], and experimental measurements [8,9]. These studies show that the predictions of RFT agree well with their findings provided that the drag coefficients appearing in RFT are calibrated properly. However, it has to be noted that experimental results–RFT predictions comparison presented in reference [10] reveal that RFT might be unsatisfactory for certain geometries such as helical tails with small pitches. Nevertheless, recent studies addressing granular locomotion by RFT indicate that the use of this theory is not limited to the mechanics of micro-swimmers exclusively, see for example [11].

İ. Özdemir (✉)
Department of Civil Engineering, Izmir Institute of Technology, Gülbahçe Kampüsü, Urla, İzmir, Turkey
E-mail: izzetozdemir@iyte.edu.tr
Tel.: +90-232-750 6810
Fax: +90-232-750 6801

Referring back to potential applications of micro-swimmers, one of the major challenges that has to be addressed is the need for an effective actuation mechanism. On board power sources and actuators are of limited use due to their miniaturization limitations. As an alternative, magnetic actuation by means of an external field is considered to be a promising option which gives better control on micro-swimmers by manipulating the magnetic field from a distance [12]. Furthermore, the required intensities are quite low so that they are harmless to human cells and can be generated easily. In fact, one of the first artificial swimmers proposed in the literature used this activation mechanism [13].

RFT-based models can be solved analytically only under certain limitations on swimmer's motion [14]. The insight gained by such solutions is invaluable, but unrestricted motions of swimmer's can only be addressed by invoking numerical solution schemes [15,16]. Furthermore, the treatment of swimmers with passive deformable components, bodies with irregular geometries and/or heterogeneous/anisotropic elastic properties calls for a flexible numerical solution framework. Furthermore, almost all of these studies focus on slender beam-type structures which are typically modeled as 1-D structural elements.

Before moving further, the focus of the current work, namely RFT-based interaction models, should not mislead the interested reader about the spectrum of the available analysis tools for FSI at low Reynolds number flows. For example, a fully coupled implicit solver for the interaction of slender flexible shells and Stokes flow is presented in [17] where geometrically nonlinear elastic structural response is resolved by FEM, and BEM is used for the Stokes flow. The resulting framework has been successfully used to analyze artificial cilia and to investigate swimming direction control strategies, see [18]. However, a simpler, solely finite element-based approach would be a valuable tool to address similar problems within shorter computational times. In fact, the locality of RFT makes it a suitable formulation that can be embedded in nonlinear finite element solvers. However, to the author's knowledge, the treatment of thin shell-type flexible bodies in combination with the resistive force theory has not been addressed fully yet. The only work in this context was presented in the appendix of reference [18] in which an RFT-based analysis of a slender flexible shell was carried out. However, in this analysis, the elastic forces developing in the slender deformable body were not taken into account, and in that sense it was incomplete. It is interesting to note that even without these elastic forces, RFT-based analysis was successful (to a certain extent) in capturing the main trend obtained by a more refined solution framework used (implicitly coupled FEM-BEM approach mentioned above) within the main body of the same reference, see [18].

Therefore, a complete RFT-based treatment would be very instrumental in exploiting the potentials and characteristics of different swimming strategies such as micro-swimmers with strip-like geometries driven by external magnetic fields. These novel swimming strategies [18–20] obviously require incorporation of magnetic forces with potentially varying external magnetic field (both in terms of intensity and period) which can be realized by a numerical solution framework. Therefore, embedding RFT and external magnetic field-induced forces within a nonlinear finite element solution framework would yield an efficient tool possessing the flexibilities of the finite element method.

Departing from this point, in this paper, an RFT-based one-way fluid–structure interaction problem is treated within a nonlinear finite element solution framework for strip-like thin structures. The contribution of the viscous forces to the force balance and to the tangent stiffness of the system is accounted consistently by introducing 'RFT elements.' Similarly, the body couples induced by the external magnetic field are introduced, and the associated tangent stiffness contribution is taken into account. The implementation is realized within the commercial FE software ABAQUS through the user element subroutine (UEL) which supports that RFT can be embedded in an existing nonlinear FE solver in a straightforward manner. It has to be noted that there exists a similarity between viscous forces introduced by RFT and displacement-dependent external forces (follower forces) confronted in, for example, shell-type structures bearing fluid pressure [21]. However, in case of RFT, not only the directions but also the magnitudes of the tractions are configuration dependent. Therefore, RFT-induced viscous forces do not fit to the classical definition of 'follower forces' typically implemented in commercial FE solvers.

The paper is organized as follows. In the next section, RFT is addressed very briefly, and the resulting viscous forces are put forward. Furthermore, body couples induced by an externally applied magnetic field on slender bodies are introduced. In the following section, viscous and magnetic forces are embedded within the weak form of linear momentum equation, and both spatial and temporal discretization schemes are explained. A short subsection is reserved for consistent linearization of these new force terms. In Sect. 4, representative examples highlighting the effectiveness of the formulation are presented before the paper is closed by the conclusion and outlook section.
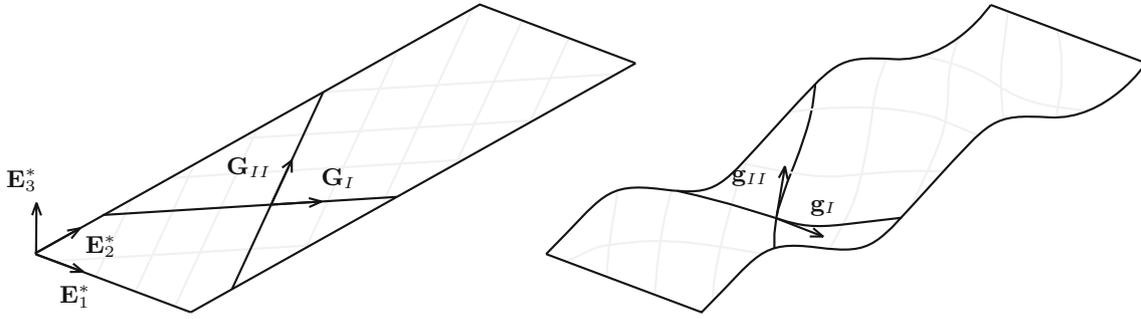
Fig. 1 A slender body within a viscous fluid is shown in undeformed and deformed configurations, respectively. *Gray lines* are the family of θ^I and θ^{II} coordinate *lines*. (Colour figure online)

2 Problem formulation

A three-dimensional thin deformable body is moving within a viscous fluid as shown in Fig. 1. The movement is typically achieved by creating bending waves along the body periodically.

For thin shell problems, an accurate and commonly used theory is based on mid-surface representation of the 3D body which is generally described by convected coordinates as shown in Fig. 1. An orthonormal vector triad $\mathbf{E}_1^*$, $\mathbf{E}_2^*$, $\mathbf{E}_3^*$ is introduced which is used to quantify in-plane and out-of-plane drag coefficients of the body. Referring to convected coordinates θ^I and θ^{II}, the tangent vector pair $\mathbf{G}_I$, $\mathbf{G}_{II}$ in the reference configuration and the corresponding pair $\mathbf{g}_I$, $\mathbf{g}_{II}$ in the current configuration are defined as

$$\mathbf{G}_I = \frac{\partial \mathbf{X}}{\partial \theta^I}, \quad \mathbf{G}_{II} = \frac{\partial \mathbf{X}}{\partial \theta^{II}}, \quad \mathbf{G}_{III} = \mathbf{G}_I \times \mathbf{G}_{II}, \tag{1}$$

$$\mathbf{g}_I = \frac{\partial \mathbf{x}}{\partial \theta^I}, \quad \mathbf{g}_{II} = \frac{\partial \mathbf{x}}{\partial \theta^{II}}, \quad \mathbf{g}_{III} = \mathbf{g}_I \times \mathbf{g}_{II} \tag{2}$$

where $\mathbf{G}_{III}$ and $\mathbf{g}_{III}$ are the normal vectors of the surface at the point of interest in the reference and current configuration, respectively. Similarly, $\mathbf{X}$ and $\mathbf{x}$ are the position vectors in the corresponding configurations. The dual contravariant basis vectors $\mathbf{G}^I$, $\mathbf{G}^{II}$ and $\mathbf{g}^I$, $\mathbf{g}^{II}$ are defined as,

$$\mathbf{G}^i = M^{ij}\mathbf{G}_j \text{ with } M^{ij} = (M_{ij})^{-1} \text{ and } M_{ij} = \mathbf{G}_i \cdot \mathbf{G}_j \text{ for } i, j = I, II, III, \tag{3}$$

$$\mathbf{g}^i = m^{ij}\mathbf{g}_j \text{ with } m^{ij} = (m_{ij})^{-1} \text{ and } m_{ij} = \mathbf{g}_i \cdot \mathbf{g}_j \text{ for } i, j = I, II, III. \tag{4}$$

At any point on the surface, body-attached orthonormal local triads are constructed via

$$\mathbf{e}_I^0 = \frac{\mathbf{G}_I}{\parallel \mathbf{G}_I \parallel}, \quad \mathbf{e}_{III}^0 = \frac{\mathbf{G}_{III}}{\parallel \mathbf{G}_{III} \parallel}, \quad \mathbf{e}_{II}^0 = \mathbf{e}_{III}^0 \times \mathbf{e}_I^0, \tag{5}$$

$$\mathbf{e}_I = \frac{\mathbf{g}_I}{\parallel \mathbf{g}_I \parallel}, \quad \mathbf{e}_{III} = \frac{\mathbf{g}_{III}}{\parallel \mathbf{g}_{III} \parallel}, \quad \mathbf{e}_{II} = \mathbf{e}_{III} \times \mathbf{e}_I \tag{6}$$

where the superscript ^{0} distinguishes the fact that the triad is evaluated in the reference configuration.

2.1 Viscous drag forces

According to RFT, the drag traction exerted by the fluid on the structure is expressed as

$$\mathbf{t} = -\mathbf{C}\,\mathbf{v} \tag{7}$$

where $\mathbf{C}$ is a resistance tensor, and $\mathbf{v}$ is the instantaneous velocity at the point of interest. If a flat slender body is translated parallel to its in-plane axes ($\mathbf{E}_1^*$ and $\mathbf{E}_2^*$ directions in Fig. 1), the drag felt would be much smaller when it is translated along $\mathbf{E}_3^*$ direction. Therefore, the resistance tensor has an anisotropic structure and can be expressed as

$$\mathbf{C}^* = C^1(\mathbf{E}_1^* \otimes \mathbf{E}_1^*) + C^2(\mathbf{E}_2^* \otimes \mathbf{E}_2^*) + C^3(\mathbf{E}_3^* \otimes \mathbf{E}_3^*) \tag{8}$$

where C^1, C^2, and C^3 are the drag coefficients in $\mathbf{E}_1^*$, $\mathbf{E}_2^*$ and $\mathbf{E}_3^*$ directions, respectively. Here it is assumed that the resistances in orthogonal directions are uncoupled. It is more convenient to express the resistance tensor with respect to $\mathbf{e}_I^0$, $\mathbf{e}_{II}^0$, $\mathbf{e}_{III}^0$ basis, which can be realized by $\mathbf{C} = \mathbf{T}\mathbf{C}^*\mathbf{T}^T$ where $\mathbf{T}$ is the transformation tensor linking the two orthogonal vector triads. Since $\mathbf{C}^*$ is a diagonal tensor, the resulting transformed tensor $\mathbf{C}$ is also diagonal with the drag coefficients C_I, C_{II}, and C_{III} appearing on the diagonal. Due to the convective nature of $\mathbf{e}_{I,II,III}^0$ and $\mathbf{e}_{I,II,III}$ vector triads, the resistance tensor has a diagonal structure in the current configuration with identical drag coefficient values on the diagonal. In other words, push forward of the resistance tensor $\mathbf{C}^*$ does not effect the drag coefficients. The drag traction can then be written as

$$\mathbf{t} = -C_I(\mathbf{v} \cdot \mathbf{e}_I)\mathbf{e}_I - C_{II}(\mathbf{v} \cdot \mathbf{e}_{II})\mathbf{e}_{II} - C_{III}(\mathbf{v} \cdot \mathbf{e}_{III})\mathbf{e}_{III} \tag{9}$$

where the terms in parentheses are the projections of the velocity vector onto $\mathbf{e}_I$, $\mathbf{e}_{II}$ and $\mathbf{e}_{III}$ directions, respectively. In fact, anisotropic drag which is locally opposite to the velocity is the source of propulsion. In other words, fluid drag is used to generate thrust provided that the space- and time-averaged propulsive force is nonzero, [3]. With a carefully selected sequence of body movements, the resultant of the drag tractions along the body could be nonzero and pointing in the direction of the desired translation. More precisely, the traction distribution along the whole body and a full cycle of the (periodic) motion has to be considered. In fact, if the sequence of body shapes when it is recorded from start to end is identical to the sequence obtained from end to start of the cycle (reciprocal motion), the body is not going to make a net translation as proved by Purcell and called as the Scallop theorem, see [2].

2.2 Magnetically induced forces

An externally applied magnetic field has been used to induce propulsion on elastic and partially magnetic rod-like and planar structures in viscous fluids, see for example [23]. The key factor of propulsion is the symmetry breaking chiral shape which is a result of the torque induced by the external magnetic field, elasticity of the flexible body and the viscous forces exerted by the surrounding fluid. A typical layout of such a micro-swimmer is shown in Fig. 2. The magnetic portion of the structure has a certain remnant magnetization direction designated by $\mathbf{m}$. When an external magnetic field $\mathbf{b}$ is applied, magnetic body couples $\mathbf{n} = \mathbf{m} \times \mathbf{b}$ develop on the magnetic portion of the structure, and due to the resistive viscous forces and elasticity of the structure, a chiral shape forms. Therefore, by controlling the external magnetic field and characteristics of the flexible structure, one can control the propulsion of the body. In fact, as demonstrated by [18], it is possible to control the swimming direction by using a thin strip with magnetically sensitive parts located at both ends as shown in Fig. 2. This case is going to be re-examined in the examples section. The resulting magnetic body couples $\mathbf{n}$ are treated as external moments acting on the body. As demonstrated in [22], magnetic interactions between the two ends are small in case of thin structures and can be ignored.
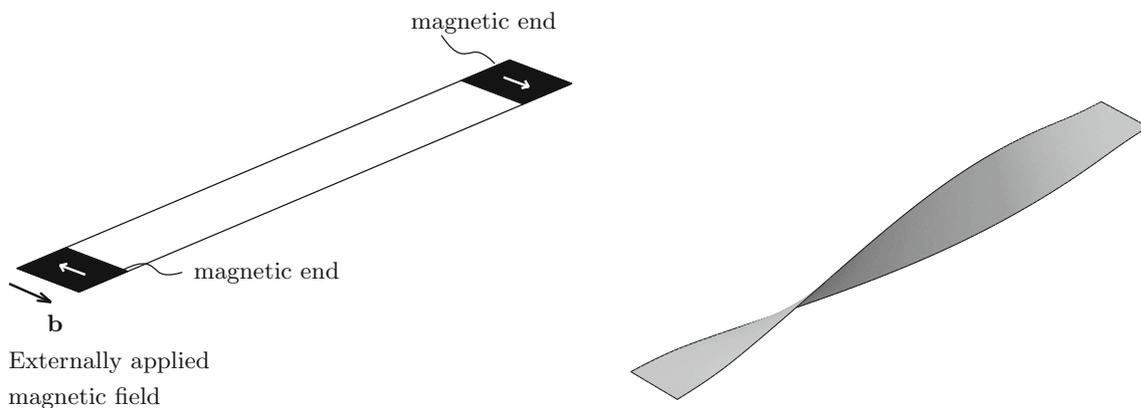
Fig. 2 Magnetically driven elastic slender body. The *white arrow* indicates the remnant magnetization direction. The magnetic portion of the body tends to align with the external magnetic field. The chiral shape develops as a result of viscous forces exerted by the surrounding fluid and the elasticity of the slender body. (Colour figure online)

3 Weak form and discretization

In a geometrically nonlinear setting, the principle of virtual work for a mid-surface-based thin shell is written as

$$\delta W^{\text{int}} - \int_V \rho(\mathbf{b}^* - \dot{\mathbf{v}}) \cdot \delta\mathbf{u} \, dv - \underbrace{\int_A \mathbf{t}^d \cdot \delta\mathbf{u} \, dA}_{\delta W^d} - \underbrace{t_0 \int_A \mathbf{n} \cdot \delta\boldsymbol{\phi} \, dA}_{\delta W^m} = 0 \qquad (10)$$

where δW^{int} is the virtual work done by the resultant internal forces, and its specific form depends on the shell theory used. $\mathbf{b}^*$ represents the body force vector, and $\dot{\mathbf{v}}$ (dot over a quantity designates differentiation with respect to time) is the acceleration field within the body. The integrals are referring to the current configuration, therefore A is the current mid-surface area, and V is the current volume of the body. δW^d is the virtual work done by the viscous drag tractions, and δW^m represents the virtual work done by the magnetic body couples over the virtual rotation field $\delta\boldsymbol{\phi}$. Although finite rotations are not vectorial quantities, typically a vector-like parameterization and notation are used, see [24]. In the treatment of the last term, it is assumed that the thickness change is small so that the current thickness t is equal to the initial thickness t_0, and therefore the volume integral can be represented by the product of initial thickness and an integral over the current mid-surface area. By introducing this approximation, both δW^d and δW^m terms can be treated within a single user element definition.

In the following subsections, the treatment of the last two terms, namely δW^d and δW^m, is going to be detailed since the treatment of other terms is not within the scope of this work and can be found for example in [21] and [24].

3.1 Spatial discretization

Although the following formulation can be adapted for any order and topology of finite strain mid-surface-based shell elements, it is assumed that the discretization is done by 4-noded isoparametric shell elements. Each node has 3 translational ($\hat{\underline{u}}_I$) and 3 rotational ($\hat{\underline{\phi}}_I$) degrees of freedom.

Referring to Fig. 3, the isoparametric coordinates ξ and η are adopted as the convected coordinates θ^I and θ^{II}, respectively. Reference and current position, displacement and velocity vectors are all based on the mid-surface and approximated by
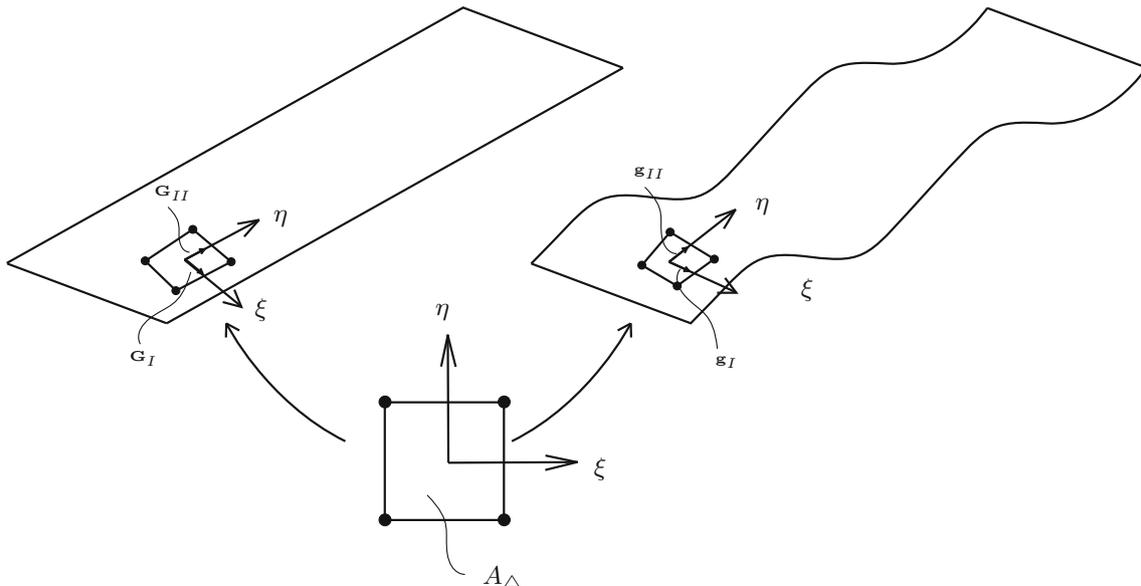
Fig. 3 Typical element in reference and current configurations. The parent element for isoparametric mapping is shown as well

$$\underline{X} = \sum_{I=1}^{4} N_I \underline{\hat{X}}_I, \quad \underline{x} = \sum_{I=1}^{4} N_I \underline{\hat{x}}_I, \quad \underline{u} = \sum_{I=1}^{4} N_I \underline{\hat{u}}_I, \quad \underline{v} = \sum_{I=1}^{4} N_I \underline{\hat{v}}_I \tag{11}$$

where N_I are the Lagrangian shape functions. Therefore, the tangent vector pairs $\{\underline{G}_I, \underline{G}_{II}\}$ and $\{\underline{g}_I, \underline{g}_{II}\}$ are simply expressed as

$$\underline{G}_I = \underline{X}_{,\xi} = \sum_{I=1}^{4} N_{I,\xi} \underline{X}_I, \quad \underline{G}_{II} = \underline{X}_{,\eta} = \sum_{I=1}^{4} N_{I,\eta} \underline{X}_I, \tag{12}$$

$$\underline{g}_I = \underline{x}_{,\xi} = \sum_{I=1}^{4} N_{I,\xi} \underline{x}_I, \quad \underline{g}_{II} = \underline{x}_{,\eta} = \sum_{I=1}^{4} N_{I,\eta} \underline{x}_I. \tag{13}$$

On the basis of $\underline{g}_I$ and $\underline{g}_{II}$, one can construct the orthonormal triad attached to any point within the element using the relations given by Eqs. (5) and (6). δW^d can be expressed explicitly as

$$\delta W^d = \int_A [C_I(\mathbf{e}_I \otimes \mathbf{e}_I) + C_{II}(\mathbf{e}_{II} \otimes \mathbf{e}_{II}) + C_{III}(\mathbf{e}_{III} \otimes \mathbf{e}_{III})] \mathbf{v} \cdot \delta \mathbf{u} \, dA. \tag{14}$$

Introducing an identical discretization for the virtual displacement field $\delta \mathbf{u}$, one can convert δW^d into the following form:

$$\delta W^d = \delta \underline{u} \int_A \underline{N}^T \left[C_I \underline{E}_I + C_{II} \underline{E}_{II} + C_{III} \underline{E}_{III} \right] \underline{N} \, \hat{\underline{v}} J dA_{\triangle} = \delta \underline{\hat{u}}^T \underline{f}^d \tag{15}$$

where $\delta \underline{\hat{u}}^T = [\delta u_x^1 \ \delta u_y^1 \ \delta u_z^1 \ \dots \ \delta u_x^4 \ \delta u_y^4 \ \delta u_z^4]$, $\hat{\underline{v}}^T = [v_x^1 \ v_y^1 \ v_z^1 \ v_x^2 \ v_y^2 \ \dots \ v_x^4 \ v_y^4 \ v_z^4]$, and $J = \| \mathbf{g}_1 \times \mathbf{g}_2 \|$. $\underline{E}_I$, $\underline{E}_{II}$ & $\underline{E}_{III}$ are the Cartesian component matrices of the dyadic products, e.g., $(E_I)_{ij} = (e_I)_i (e_J)_j$, and the others are defined similarly. The explicit form of δW^m reads

$$\delta W^m = t_0 \int_A m(\mathbf{q} \times \mathbf{b}) \cdot \delta \boldsymbol{\phi} \, dA \tag{16}$$

where m is the intensity of the remnant magnetization and $\mathbf{q}$ is the unit vector in the direction of magnetization in the current configuration. Since the magnetization vector $\mathbf{q}$ is a material vector, it is defined as

$$\mathbf{q} = \frac{\mathbf{F} \mathbf{q}_0}{\|\mathbf{F} \mathbf{q}_0\|} \tag{17}$$

where $\mathbf{q}_0$ is the initial magnetization unit vector and $\mathbf{F}$ is the deformation gradient tensor of the mid-surface defined as $\mathbf{F} = \sum_{i=1}^{3} \mathbf{g}_i \otimes \mathbf{G}^i$. Introducing an identical linear interpolation for $\delta \boldsymbol{\phi}$, δW^m takes the following discrete form:

$$\delta W^m = m \, t_0 \, \delta \hat{\underline{\phi}} \int_A \underline{N}^T \hat{\underline{q}} \, \underline{b} \, J \, dA_{\triangle} = \delta \hat{\underline{\phi}} \, \underline{f}^m \tag{18}$$

where $\hat{\underline{q}}$ is the matrix form of the skew-symmetric tensor such that $\mathbf{q} \times \mathbf{b} = \hat{\underline{q}} \, \underline{b}$. Obviously the nodal force columns $\underline{f}^d$ and $\underline{f}^m$ have to be taken into account in the force balance.

The integrals in Eqs. (15) and (16) are evaluated by Gauss integration with four integration points per element. The dependency of drag forces on $\mathbf{v}_{n+1}$ is obvious from δW^d, and the dependency of drag and magnetic forces on $\Delta \mathbf{u}$ (or $\mathbf{u}_{n+1}$) stems from the fact that the body-attached local triad and $\mathbf{q}$ are both motion dependent. The fully discrete equilibrium equations are obtained upon temporal discretization, and the resulting system of nonlinear equations is solved by the Newton–Raphson method. Therefore, consistent linearization is necessary which is going to be briefly mentioned following the temporal discretization summarized in the next subsection.

3.2 Temporal discretization

On the time axis, the discretization is realized by using the Hilber-Hughes-Taylor integration scheme [25]. Velocity proportional drag forces can be treated similar to the damping term appearing in classical structural dynamics problems. Therefore, in a fully discrete form $\underline{f}^d$ at time step n+1 reads

$$\underline{f}^d_{n+1} = \int_A \underline{N}^T \left[C_I \underline{E}_I + C_{II} \underline{E}_{II} + C_{III} \underline{E}_{III} \right] \underline{N} \, \hat{\underline{v}}_{n+1} J dA_\triangle. \tag{19}$$

Obviously, $\underline{f}^m_{n+1}$ enters the system of equations as an externally applied force column. As presented concisely in the next subsection, the linearization procedure requires partial derivatives of both $\underline{f}^d_{n+1}$ and $\underline{f}^m_{n+1}$ with respect to nodal displacements. To this end, the following equalities of Hilber-Hughes-Taylor integration scheme,

$$\frac{d\dot{\mathbf{v}}}{d\mathbf{u}} = \frac{1}{\beta \Delta t^2}, \quad \frac{d\mathbf{v}}{d\mathbf{u}} = \frac{\gamma}{\beta \Delta t}, \tag{20}$$

are used. The variables $\beta = 1/4(1-\alpha)^2$ and $\gamma = 1/2 - \alpha$ are the parameters of the integration scheme where the numerical dissipation is controlled by α; $-1/3 \le \alpha \le 0$. For details one can consult reference [25].

3.3 Consistent linearization

The directional derivative of δW^d in the direction of incremental displacements $\Delta\mathbf{u}$ can be split into two parts,

$$D[\delta W^d][\Delta\mathbf{u}] = \int_{A_\triangle} D\left[J \, \tilde{\mathbf{C}} \right] [\Delta\mathbf{u}] \, \mathbf{v} \cdot \delta\mathbf{u} \, dA_\triangle + \int_{A_\triangle} (J \, \tilde{\mathbf{C}}) D\mathbf{v} \, [\Delta\mathbf{u}] \cdot \delta\mathbf{u} \, dA_\triangle$$

$$\text{with } \tilde{\mathbf{C}} = C_I \, (\mathbf{e}_I \otimes \mathbf{e}_I) + C_{II} \, (\mathbf{e}_{II} \otimes \mathbf{e}_{II}) + C_{III} \, (\mathbf{e}_{III} \otimes \mathbf{e}_{III}), \tag{21}$$

where $D [\,] [\Delta\mathbf{u}]$ is the directional derivative of the term in square brackets in the direction of $\Delta\mathbf{u}$. With the aid of Eq. (20), the derivative of $\mathbf{v}$ can simply be expressed as

$$D\mathbf{v} \, [\Delta\mathbf{u}] = \frac{\gamma}{\beta \Delta t} \Delta\mathbf{u}. \tag{22}$$

The linearization of the dyadic product $\mathbf{e}_I \otimes \mathbf{e}_I$ reads

$$D \, [\mathbf{e}_I \otimes \mathbf{e}_I] = D\mathbf{e}_I \, [\Delta\mathbf{u}] \otimes \mathbf{e}_I + \mathbf{e}_I \otimes D\mathbf{e}_I \, [\Delta\mathbf{u}], \tag{23}$$

$$\text{with } D\mathbf{e}_I \, [\Delta\mathbf{u}] = \frac{1}{\| \mathbf{g}_I \|} \, (\mathbf{I} - \mathbf{e}_I \otimes \mathbf{e}_I) \, \Delta\mathbf{u}_{,I}, \tag{24}$$

and directional derivatives of $\mathbf{e}_{II} \otimes \mathbf{e}_{II}$, $\mathbf{e}_{III} \otimes \mathbf{e}_{III}$ and J can be carried out similarly.

As far as linearization of δW^m is concerned, directional derivatives in the direction of $\Delta\boldsymbol{\phi}$ and $\Delta\mathbf{u}$ have to be considered. Therefore, the following explicit forms are obtained,

$$D \left[\delta W^m \right] [\Delta\mathbf{u}] = t_0 \int_{A_\triangle} m \, (D\mathbf{q} \, [\Delta\mathbf{u}] \times \mathbf{b}) \cdot \delta\boldsymbol{\phi} \, J \, dA_\triangle$$

$$+ t_0 \int_{A_\triangle} m \, (\mathbf{q} \times \mathbf{b}) \cdot \delta\boldsymbol{\phi} \, DJ \, [\Delta\mathbf{u}] \, dA_\triangle, \tag{25}$$

$$D \left[\delta W^m \right] [\Delta\boldsymbol{\phi}] = t_0 \int_{A_\triangle} m \, (\mathbf{q} \times \mathbf{b}) \cdot D \, [\delta\boldsymbol{\phi}] \, [\Delta\boldsymbol{\phi}] \, J \, dA_\triangle \tag{26}$$

where $D \, [\delta\boldsymbol{\phi}] \, [\Delta\mathbf{u}] = -\frac{1}{2} \delta\boldsymbol{\phi} \times \Delta\boldsymbol{\phi}$ due to the nonvectorial nature of finite rotations; for details one can consult reference [26]. It can be shown that the directional derivative of $\mathbf{q}$ results in

$$D\mathbf{q} \, [\Delta\mathbf{u}] = \frac{1}{||\mathbf{Fq}_0||} (\mathbf{I} - \mathbf{q} \otimes \mathbf{q}) D\mathbf{F} \, [\Delta\mathbf{u}] \, \mathbf{q}_0, \tag{27}$$

and the evaluation of $D\mathbf{F} \, [\Delta\mathbf{u}]$ can be realized in a rather straightforward manner by $D\mathbf{F} \, [\Delta\mathbf{u}] = \sum_{i=1}^{3} D\mathbf{g}_i \, [\Delta\mathbf{u}] \otimes \mathbf{G}^i$.

4 Examples

The presented formulation is implemented in ABAQUS 6.14 through user element (UEL) subroutine [27]. In the following subsections, representative numerical examples are presented demonstrating the capabilities of the formulation. For all cases, a 4-node large strain shell element (ABAQUS element type S4) is used for the discretization of the thin body, and numerical damping is introduced by choosing $\alpha = -0.05$.

4.1 Swimming sheet

The translation of a waving sheet in Stokes flow was addressed by Taylor [4], and an analytical solution for the swimming velocity in terms of wave amplitude b and wavelength λ was derived as

$$V_s = \sigma k b^2 \left(\frac{\xi - \eta}{\eta} \right) \text{ with } \sigma = k V_w \text{ and } k = 2\pi/\lambda \tag{28}$$

where V_w is the wave velocity; ξ and η are the in-plane and out-of-plane drag coefficients, respectively.

In this example, a 0.1-mm-thick flat rectangular shell of 2 mm by 20 mm is considered which uses the same strategy to translate in the surrounding viscous fluid. An undulating body profile is imposed by a transverse displacement field of the form

$$\Delta = b \sin \left(k \left(Z - Z_0 \right) + V_w t \right) \tag{29}$$

by means of the user-defined boundary condition capability of ABAQUS, [27]. The coordinates are taken as the reference coordinates, and Z_0 is the corresponding coordinate of the front end of the shell, see Fig. 3. The material constants, drag coefficients, parameters of Eq. (29), and the details of different discretizations realized are given in Table 1.

In Fig. 4, the translated configuration of the body by undulating body waves is shown, and in Fig. 5 time versus Z-displacement of the front node [highlighted in red (corner node) in Fig. 4] for three different discretizations is presented along with the analytical result based on Eq. (28). After the initial transient phase (the inset on the left upper corner) the curves clearly reach a steady-state profile from which an average velocity

Table 1 Material constants, drag coefficients, motion parameters, the three discretizations (M#1, M#2 and M#3) realized.

E (MPa)	ν	ρ (kg/mm^3)	$C^{1,2}$ (N s/m^2)	C^3 (N s/m^2)	
100	0.3	0.00001	3.0	5.67	
b (mm)	k	V_w (mm/s)	$M \# \text{I}$	$M \# \text{II}$	$M \# \text{III}$
0.15	0.5	200	4×20	4×50	4×100
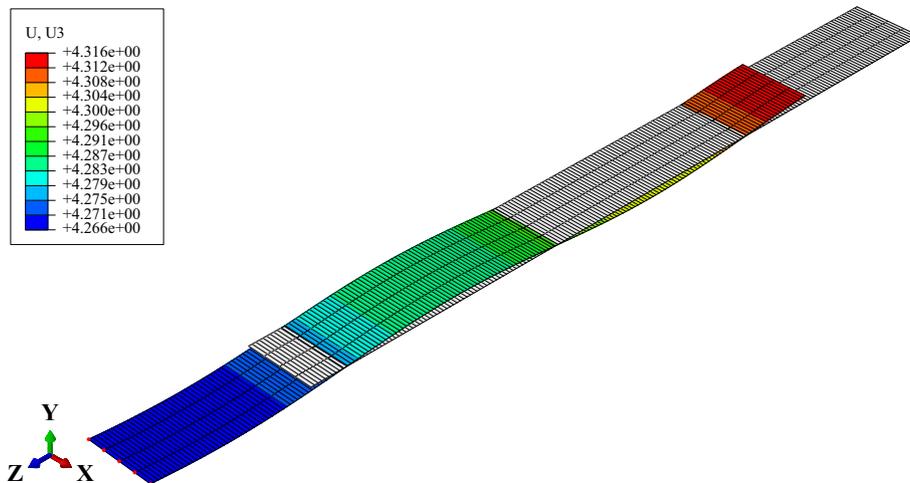
Fig. 4 Initial (*gray*) and final configuration of a swimming sheet. Contours represent displacement in Z-direction in mm's. Nodes located at the front end are highlighted in *red*. (Colour figure online)
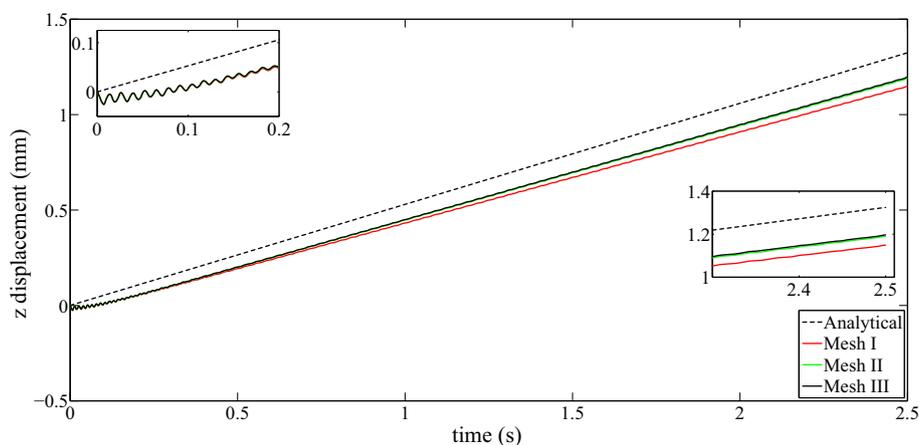
Fig. 5 Time–displacement graphs for different discretizations and the analytical solution. Initial transient response is visible in the *upper left inset*, and the convergence trend and the characteristic wavy displacement response is visible in the *lower right inset*

Table 2 Swimming sheet: problem data and swimming velocities for different cases and analytical velocity given by (28) (material parameters and drag coefficients are identical to the ones given in Table 1)

Parameters	b (mm)	k	V_w (mm/s)	Mesh	V_s (mm/s)	V_s^A
Case I	0.15	0.5	200	Mesh #1	0.4780	0.5298
Case II	0.15	0.5	200	Mesh #2	0.4951	0.5298
Case III	0.15	0.5	200	Mesh #3	0.4975	0.5298
Case IV	0.15	0.5	400	Mesh #2	0.9885	1.0595
Case V	0.075	0.5	400	Mesh #2	0.2479	0.2649

can be calculated. To exclude the effect of the initial transient phase, average velocity calculation is based on displacement data at $t = 1.5$ and $t = 2.0$ s.

The comparison of numerical predictions and the analytical result given in Table 2 indicates that for reasonable discretizations (e.g., mesh #2) the error is about 6%. Furthermore, the analytical solution given by Eq. (28) contains some valuable scaling information on the swimming velocity as a function of body waving parameters. To assess such capabilities of this numerical framework, two other cases are considered as summarized in Table 2. The linear dependence on waving velocity ($V_s^{\text{Case IV}}/V_s^{\text{Case II}} = 1.9966$) and quadratic dependence on wave amplitude ($V_s^{\text{Case V}}/V_s^{\text{Case IV}} = 3.9875$) are reproduced accurately as can be deduced from Table 2.

4.2 Three-link swimmer

One of the simplest geometries that can achieve net translation in a viscous fluid is a three-link swimmer. In this example, a three-link swimmer consisting of three thin sheets as shown in Fig. 6 is considered. The components are identical in dimensions ($L = 5$ mm by $W = 0.5$ mm and the thickness $t = 0.2$ mm), and the arms are connected by hinges allowing rotations around X-axis to the middle sheet. These connections are realized by using proper ties between corresponding degrees of freedom of the nodes sharing the same position along the joining line.

A set of different cases are considered in this example as well, and the corresponding data are tabulated in Table 3. Scallop theorem [2] states that for a three-link swimmer with rigid arms a time-reversible motion history (reciprocal motion) does not yield any net translation. In order to check the validity of the current formulation, in the first case, the motion of a three-link swimmer with very stiff arms is considered.

The imposed displacement history of the end nodes of left and right arms (in the Y-direction) is also sketched in Fig. 6 which is time symmetric. In other words, the sequence of motions as played from start to end and the sequence from end to start are indifferent. In Fig. 7, the resulting motion of the reference corner in Z-direction is plotted as a function of time.
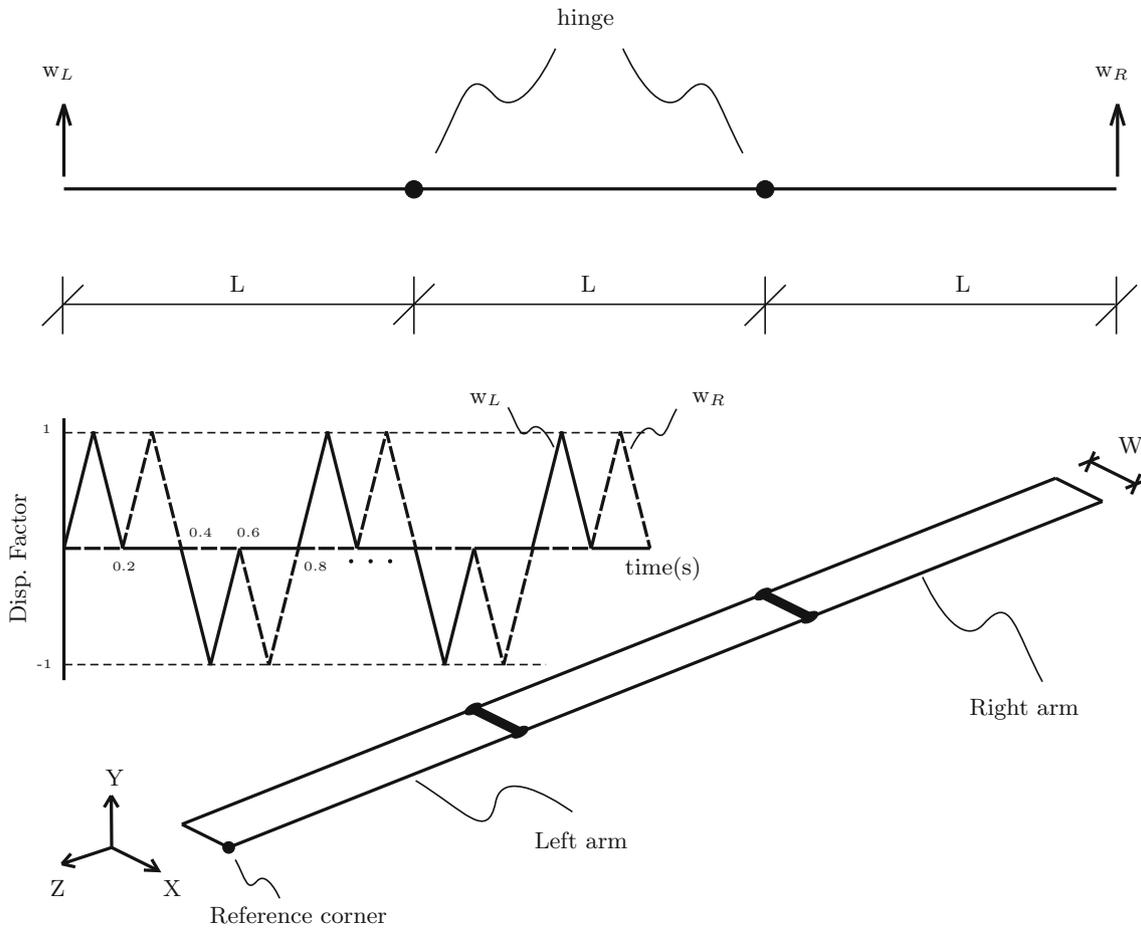
Fig. 6 Side view (*top*) and perspective view (*bottom*) of a three-link swimmer. Time histories of prescribed w_L and w_R are also given.

Table 3 Three-link swimmer: subscripts L, M, and R stand for left, right and middle, respectively

Parameters	E_L (MPa)	E_M (MPa)	E_R (MPa)	BC's
Case I	400	400	400	w_L & w_R
Case II	40	40	400	w_L & w_R
Case III	40	40	400	w_L
Case IV	4	4	400	w_L

Other material constants and drag coefficients are identical to the ones given in Table 1

In order to investigate the net translation of the body, in Table 4, the z-displacement of the reference node at equal time intervals is tabulated. Due to the dynamic and initiallly transient nature of the motion, at the end of the first cycle ($t = 0.4$ s) there is a net movement of the body. However, as seen from the Table, the change in displacement is very small (as compared to the in-plane dimensions of the three components and typical values obtained by unsymmetrical systems considered in the sequel) from cycle to cycle. The cyclic motion is repeating itself, and the net movement is not growing in a significant manner and consistent with the scallop theorem.

In order to break the symmetry in the system, the stiffness of the left (E_L) and middle arms (E_M) reduced to one-tenth of the right arm (E_R), see case II in Table 3. As shown in Fig. 8, the swimmer starts to gain net translation at the end of each cycle. When the boundary condition on the right arm is removed (corresponds to case III in Table 3), both the amount of net translation and the cyclic characteristics of the movement are changing. Referring to case IV in Table 3, decreasing the stiffness of left and middle arms results in an increased net translation and a different signature of the movement. Obviously, finite element-based modeling allows one
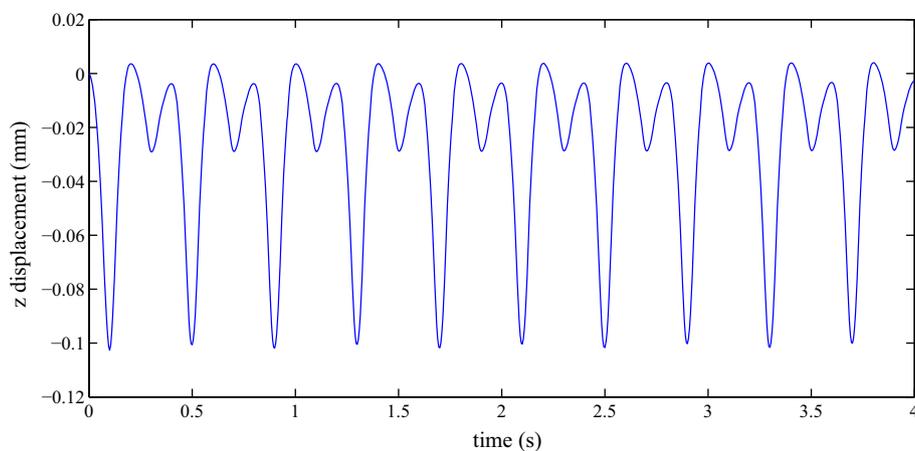
Fig. 7 Time history of z-displacement of the reference corner (see Fig. 5)

Table 4 Numerical values of the displacement of the reference corner (see Fig. 5)

Time (s)	Position (mm)
0.4	−0.003758
0.8	−0.003759
1.2	−0.003650
1.6	−0.003648
2.0	−0.003535
2.4	−0.003537
2.8	−0.003420
3.2	−0.003427
3.6	−0.003305
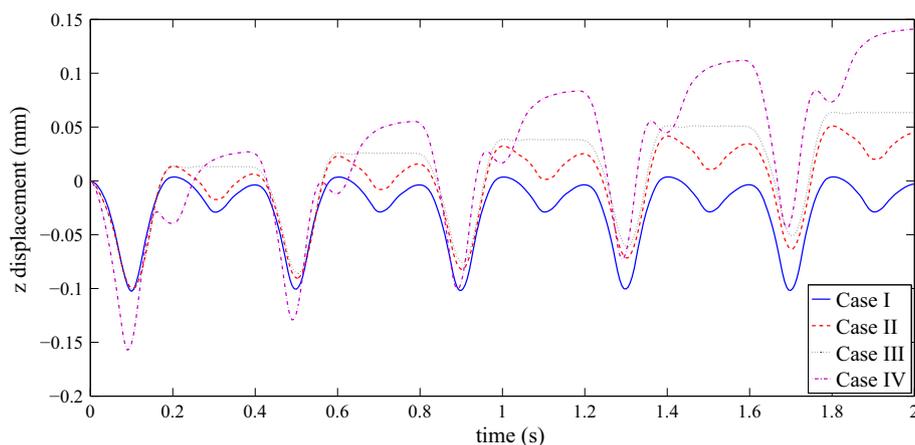
Fig. 8 Three-link swimmer: z-displacement of the reference corner (see Fig. 5) for different cases. The net displacements for unsymmetrical systems are clearly visible

to test different possibilities in a straightforward manner. Embedding this framework within an optimization loop might yield much efficient swimming strategies and layouts in terms of geometry and material property distribution.

4.3 Bidirectional swimming of flexible strips

Magnetically driven flexible micro-swimmers are considered to be good candidates for certain applications in micro-fluidics. A novel layout recently proposed by Namdeo and his colleagues [18] is shown on the left-hand
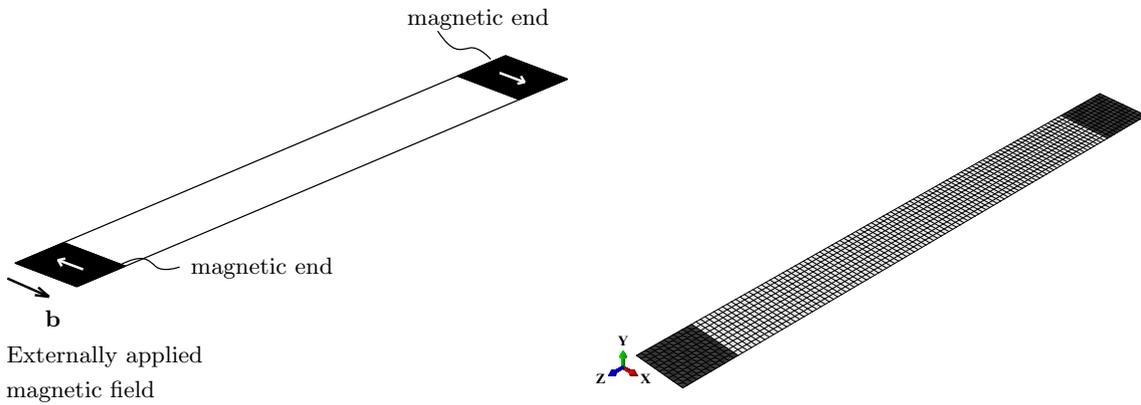
Fig. 9 Magnetically driven elastic slender body. The *white arrows* indicate the remnant magnetization directions. A discretized strip (10 by 120 divisions) is shown on the *right*-hand side. (Colour figure online)
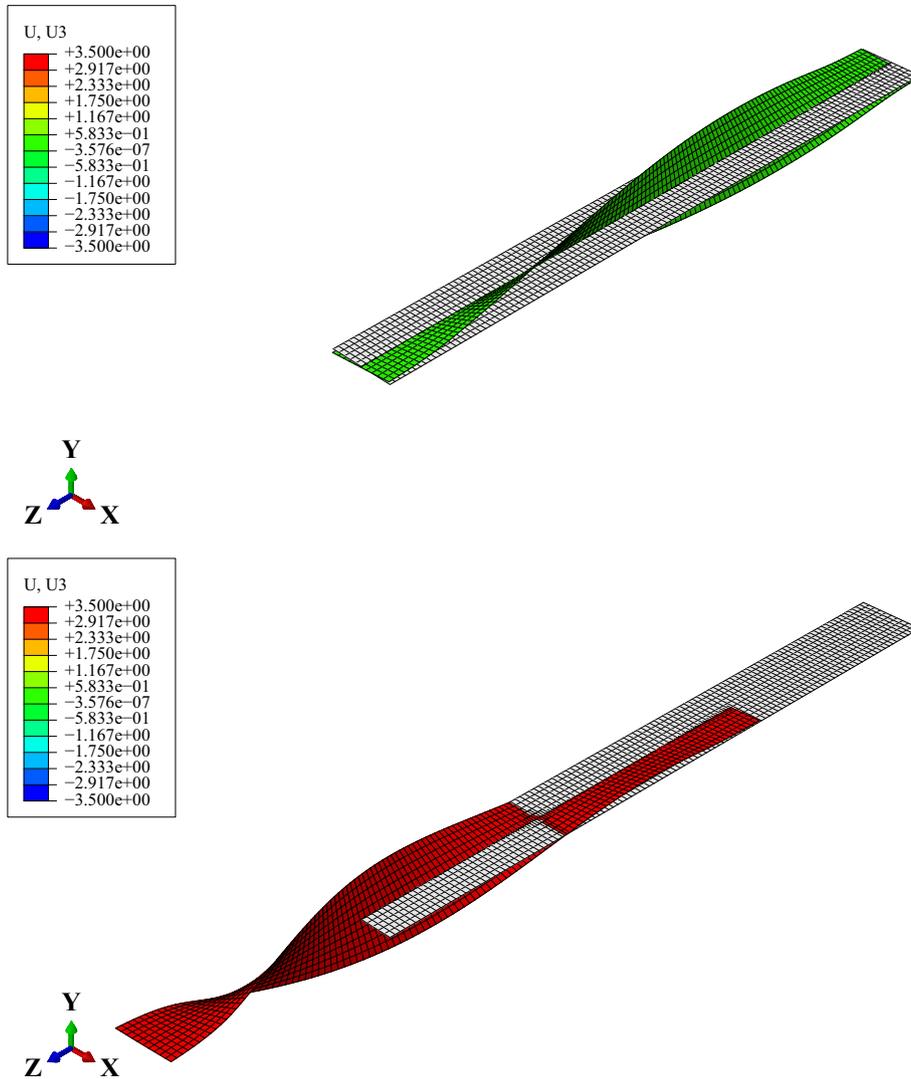
Fig. 10 Magnetically driven elastic slender body in forward motion for $f = 4$ 1/s. Contours represent displacement in Z-direction in mm's
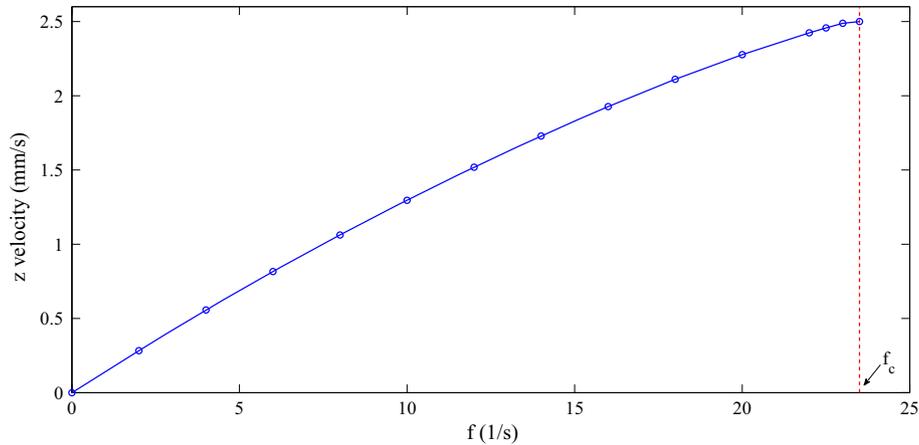
Fig. 11 Swimming velocities at different rotation frequencies of the external magnetic field

side of Fig. 9. The ends of the strip are magnetically sensitive with a remnant magnetization direction and tends to align itself parallel to the externally applied magnetic field. Therefore, as a result of internal forces, viscous drag forces and the magnetic body couples, a chiral shape similar to a helix develops, and upon rotation of the magnetic field, the strip translates. This particular form is designed to control/reverse the swimming direction on the fly just by reversing the externally applied magnetic field. In this approach, the external magnetic loading is decomposed into two phases.

In the first phase, the external magnetic field is positioned such that one of the magnetic ends of the strip twists, while the other end keeps their configuration. Labeling the magnetic ends as end 1 and end 2 for the sake of discussion, in the first phase the external magnetic field is kept parallel to end 2 which results in twisting of end 1 until it gets parallel to end 2. A chiral shape forms at the end of this phase. In the second phase of loading, the magnetic field is rotated with a certain frequency, and since both ends have almost parallel magnetization directions, the strip translates as the external magnetic field rotates. If the magnetic field is reversed and the same loading protocol is followed, end 2 twists until it gets parallel to end 1, and upon rotation of the magnetic field, the strip translates in the opposite direction.

To investigate this strategy numerically with the proposed framework, a 0.1-mm-thick rectangular strip of 10 mm by 2 mm is considered. The length of the magnetic parts is 1 mm in length at both ends, and the strip is discretized by 1200 S4 elements, see Fig. 9. The drag coefficients are the same as the values given in Table 1, and the elasticity constants for the strip are $E = 5$ Mpa and $\nu = 0.3$. Density is taken to be $\rho = 1600$ kg/m^3, and the remnant magnetization of the ends of the strip is 0.0629 kA/mm. These values are based on the data used in reference [19], and the drag coefficients are of the same order of the values used in [16].

The remnant magnetization directions for end 1 and end 2 are not perfectly parallel to X and -X directions, and their rectangular components read as (0.995, 0.0995, 0.0) and (0.995, 0.0995, 0.0), respectively. These initial imperfections are introduced to induce twisting of the relevant end depending on the loading protocol. In the first phase of loading, the intensity of the external magnetic field is linearly increased from zero to 0.75 N/(mm A); meanwhile, its direction is kept parallel to X (or -X) direction. In the second phase, the external magnetic field is rotated following a sinusoidal function with frequency **f** as $b = 0.75\sin(2\pi f t)$.

The deformed shape at the end of phase I and at the end of phase II is shown in Fig. 10. Viscous forces resist the motion of the swimmer, while the magnetically sensitive end follows the rotating external magnetic field resulting in the chiral shape shown in Fig. 10. An immediate question which arises at this stage is the relation between frequency of the magnetic field and swimming velocity. To this end, the analysis is repeated with different frequencies, and the resulting swimming velocities are shown in Fig. 11.

It can be seen that the swimming velocity increases until a critical frequency f_c is reached. In the literature, see, e.g., [28], this frequency is called as the step-out frequency beyond which the swimmer's front end cannot follow the external magnetic field. For the example problem, the Z position of the swimmer for $f_c = 24$ 1/s which is larger than f_c is shown in Fig. 12.

For frequencies larger than f_c, the swimmer loses its chiral shape, and erratic tumbling motion sets in as can be deduced from Fig. 12.
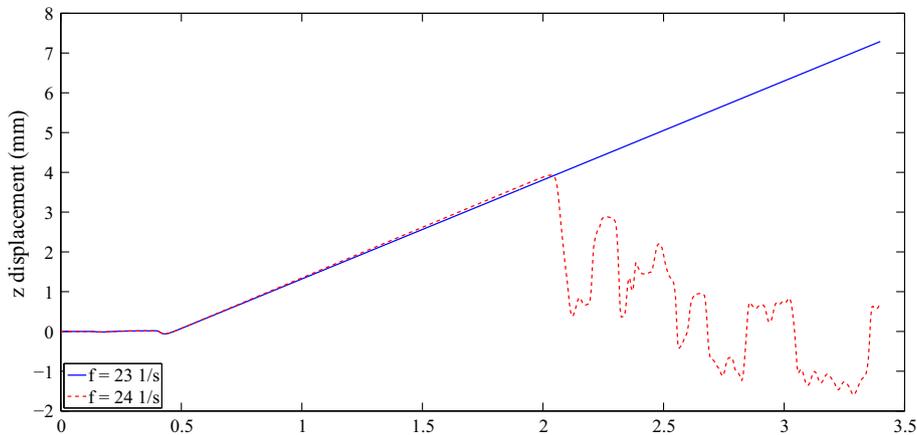
Fig. 12 Z coordinate of the swimmer for two different frequencies

5 Conclusions and outlook

In this paper, the resistive force theory which has been used extensively for beam-type slender bodies has been adapted for thin shell-type structures. Furthermore, the formulation is enhanced by considering body couples induced by externally applied varying magnetic fields. Both viscous and magnetic forces are treated within a single user element formalism and implemented into ABAQUS.

As compared to the more refined approach presented by [17,18], the current work does not bring any further insight into the physics of the problem. On the other hand, in this work, a simpler and more accessible, purely finite element-based framework is laid out. The current formulation is most probably cheaper in terms of computational cost as compared to a fully coupled FEM-BEM formulation. It is obvious that the physical representation of the flow by RFT is weaker than the boundary element-based treatment of hydrodynamics. However, it is shown that the current formulation is also successful in capturing the nontrivial physics as exemplified by an analysis of a magnetically driven flexible micro-swimmer including an investigation on the critical frequency (step-out frequency). This result suggests that the formulation can be potentially used in design-oriented studies and can be placed within an optimization algorithm. An interesting and challenging extension would be to investigate the optimum 'loading' protocol by varying the amplitude and frequency characteristics of the externally applied magnetic field as discussed for beam-type swimmers in reference [20]. More importantly, relying on the flexibilities of the finite element method, the influence of some other parameters such as variable thickness along the body and anisotropic elasticity on the swimming performance can be investigated in an efficient way.

References

1. Gao, W., Kagan, D., Pak, O.S., Clawson, C., Campuzano, S., Chuluun-Erdene, E., Shipton, E., Fullerton, E.E., Zhang, L., Lauga, E., Wang, J.: Cargo-towing fuel-free magnetic nanoswimmers for targeted drug delivery. Small **8**, 460–467 (2012)
2. Purcell, E.M.: Life at low Reynolds number. Am. J. Phys. **45**, 3–11 (1977)
3. Lauga, E., Powers, T.R.: The hydrodynamics of swimming microorganisms. Rep. Prog. Phys. **72**, 096601 (2009)
4. Taylor, G.: Analysis of the swimming of microscopic organisms. Proc. R. Soc. A **209**, 447–461 (1951)
5. Gray, J., Hancock, J.: The propulsion of sea-urchin spermatozoa. J. Exp. Biol. **32**, 802–814 (1955)
6. Johnson, R.E., Brokaw, C.J.: A comparison between resistive force theory and slender-body theory. Biophys. J. **25**, 113–127 (1979)
7. Tabak, A.F., Yeşilyurt, S.: Computationally-validated surrogate models for optimal geometric design of bio-inspired swimming robots: Helical swimmers. Comput. Fluids **99**, 190–198 (2014)
8. Freidrich, B.M., Riedel-Kruse, I.H., Howard, J., Julicher, F.: High precision tracking of sperm swimming fine structure provides strong test of resistive force theory. J. Exp. Biol. **213**, 1226–1234 (2010)
9. Sznitman, J., Shen, X., Sznitman, R., Arratia, P.E.: Propulsive force measurement and flow behaviour of undulatory swimmers at low Reynolds number. Phys. Fluids **22**, 121901 (2010)
10. Rodenborn, B., Chen, C.-H., Swinney, H. L., Liu, B., Zhang, H. P.: Propulsion of microorganisms by a helical flagellum. In: Proceedings of the National Academy of Sciences of the United States of America, PNAS, pp. E 338–E 347, (2013)
11. Zhang, T., Goldman, D.I.: The effectiveness of resistive force theory in granular locomotion. Phys. Fluids **26**, 101308 (2014)

12. Ye, Z., Regnier, S., Sitti, M.: Rotating magnetic miniature swimming robots with multiple flexible flagella. IEEE Trans. Robot. **30**, 3–13 (2014)
13. Dreyfus, R., Baudry, J., Roper, M.L., Fermigier, M., Stone, H.A., Bibette, J.: Microscopic artificial swimmers. Nature **437**, 862–865 (2005)
14. Lauga, E.: Floppy swimming: viscous locomotion of actuated elastica. Phys. Rev. E **75**, 041916 (2007)
15. Yu, T.S., Lauga, E., Hosoi, A.E.: Experimental investigations of elastic tail propulsion at low Reynolds number. Phys. Fluids **18**, 091701 (2006)
16. Alouges, F., DeSimone, A., Giraldi, L., Zoppello, M.: Self-propulsion of slender micro-swimmers by curvature control: N-link swimmers. Int. J. Non-linear Mech. **56**, 132–141 (2013)
17. Khaderi, S.N., Onck, P.R.: Fluid-structure interaction of three-dimensional magnetic artificial cilia. J. Fluid Mech. **708**, 303–328 (2012)
18. Namdeo, S., Khaderi, S.N., Onck, P.R.: Numerical modelling of chirality-induced bi-directional swimming of artificial flagella. Proc. R. Soc. A **470**, 20130547 (2014)
19. Khaderi, S.N., Baltussen, M.G.H.M., Anderson, P.D., Ioan, D., den Toonder, J.M.J., Onck, P.R.: Nature-inspired microfluidic propulsion using magnetic actuation. Phys. Rev. E **79**, 046304 (2009)
20. Cicconofri, G., DeSimone, A.: Motion planning and motility maps for flagellar microswimmers. Eur. Phys. J. E **39**(7), 72 (2016)
21. Wriggers, P.: Nonlinear Finite Element Methods. Springer-Verlag, Berlin Heidelberg (2008)
22. Khaderi, S.N.: Nature-inspired microfluidic propulsion using magnetic artificial cilia. PhD Thesis, University of Groningen, the Netherlands, ISBN:978-90-367-5072-1 (2011)
23. Garstecki, P., Tierno, P., Weibel, D.B., Saques, F., Whitesides, G.M.: Propulsion of flexible polymer structures in a rotating magnetic field. J. Phys. Condens. Matter **21**, 204110 (2009)
24. Abaqus 6.14 Theory Guide, Dassault Systemes, (2014)
25. Hilber, H.M., Hughes, T.J.R., Taylor, R.L.: Improved numerical dissipation for time integration algortihms in structural dynamics. Earthq. Eng. Struct. Dyn. **5**, 283–292 (1977)
26. Krenk, S.: Nonlinear Modeling and Analysis of Solids and Structures. Cambridge University Press, Cambridge (2009)
27. Abaqus 6.14 User Subroutines Reference Guide, Dassault Systemes, (2014)
28. Alouges, F., DeSimone, A., Giraldi, L., Zoppello, M.: Can magnetic multilayers propel artificial microswimmers mimicking sperm cell? Soft Robot. **2**, 117–129 (2013)